Understanding Properties of Engineered Catalyst Supports using Contact Angle Measurements and X-Ray Reflectivity

Placidus B. Amama, [‡,*,a,] Ahmad E. Islam,[‡,b,c] Sammy M. Saber,[b,d] Daniel R. Huffman,[b,d] and Benji Maruyama[b]

[a]Department of Chemical Engineering, Kansas State University, Manhattan, Kansas 66506, USA. E-mail: pamama@ksu.edu; Tel: 785-532-4318; Fax: 785-532-7372

[b]Air Force Research Laboratory, Materials and Manufacturing Directorate, RXAS, Wright-Patterson AFB, Ohio 45433, USA

[c]National Research Council, National Academy of Sciences, Washington D.C. 20001, USA

[d]UES Inc., Dayton, Ohio 45432, USA

[†]Electronic supplementary information (ESI) available. See DOI:

[‡]Both authors contributed equally to this work.

ABSTRACT

There is significant interest in broadening the type of catalyst substrates that support the growth of high-quality carbon nanotube (CNT) carpets. In this study, ion beam bombardment has been utilized to modify catalyst substrates for CNT carpet growth. Using a combination of contact angle measurements (CAMs) and X-ray reflectivity (XRR) for the first time, new correlations between the physicochemical properties of pristine and engineered catalyst substrates and CNT growth behavior have been established. The engineered surfaces obtained after exposure to different degrees of ion beam damage have distinct physicochemical properties (porosity, layer thickness, and acid-base properties). CAM data were analyzed using the van Oss-Chaudhury-Good model, enabling the determination of the acid-base properties of the substrate surfaces. For XRR data, a Fourier analysis of the interference patterns enabled extraction of layer thickness while the atomic density and interfacial roughness were extracted by analyzing the amplitude of the interference oscillations. The dramatic transformation of the substrate from "inactive" to "active" is attributed to a combined effect of substrate porosity or damage depth and Lewis basicity. The results reveal that the efficiency of catalyst substrates can be further improved by increasing the substrate basicity, if the minimum surface porosity is established. This study advances the use of a non-thermochemical approach for catalyst substrate engineering, as well as demonstrates the combined utility of CAM and XRR as a powerful, nondestructive, and reliable tool for rational catalyst design.

INTRODUCTION

High-quality vertically aligned carbon nanotube (CNT) structures or "CNT carpets" of controlled properties are highly desirable in a growing number of important applications such as thermal management,[1-3] energy storage,[4-6] field emission arrays,[7,8] and ultralight weight composites.[9-11] The widely preferred method for the growth of CNT carpets is catalytic chemical vapor deposition (CVD).[12-18] An influential growth parameter during the growth process is the catalyst, usually consisting of an active phase (a thin film of Fe, Ni, or Co) deposited on either silica or an amorphous alumina supporting layer.[18-22] Catalysts supported on alumina have been widely heralded for their unparalleled efficiency in the growth of high-quality CNT carpets with hydrocarbon precursors.[20,21,23] Hitherto, extending the high CNT carpet growth efficiency observed on amorphous alumina layers[14,20,24,25] to other substrates has remained a monumental challenge,[26] and has thus become a major barrier in applications that require direct growth of CNT carpets on non-amorphous alumina substrates. The rational design of active catalysts using nontraditional substrates has been handicapped by the limited understanding of catalyst-substrate interactions and the absence of a well-established non-thermochemical tool for catalyst substrate engineering, as well as a reliable tool for rapid probing of the active site densities of catalysts.

A number of studies have been conducted to understand the role of alumina substrates in CNT carpet growth via CVD. It has been suggested that the high porosity of alumina provides diffusion channels for the dissociated carbon atoms.[24,27] During the pretreatment step, the reaction between Fe and Al_2O_3 at the interface also enhances the catalyst-substrate interactions and results in the formation of highly stable nanoparticles that have high CNT nucleation density.[20] Our previous work revealed that the activity and lifetime of Fe catalysts are maximized by using amorphous alumina substrate with higher porosity.[21,22,28] In fact, dramatic differences in CNT growth behaviors have been reported even for catalysts supported on substrates with similar chemical composition, but different surface chemistry,[19,29] porosity,[21,30] or crystal structure.[27,30,31] The aforementioned studies give credence to the highly sensitive nature of the catalyst behavior to the physicochemical properties of the substrate. Building upon our extensive investigation of CNT nucleation and growth,[21,22,28,29,32-34] we recently showed that an "inactive" catalyst substrate, c-cut sapphire (crystalline alumina), can be converted to a highly "active" substrate for CNT carpet growth via substrate engineering. The properties of the

resulting CNT carpets are at par with those obtained from amorphous alumina-supported catalysts.[30] This substrate engineering approach involved introduction of porosity at the surface via ion beam bombardment that changed the surface chemistry from an inactive to an active surface. This transformation provides an excellent model system to conduct rational modification of catalyst substrates and to investigate the substrate properties.

The physicochemical properties of pristine and ion beam damaged crystalline alumina substrates are probed using a combination of contact angle measurement (CAM) and X-ray reflectivity (XRR). The combined approach is facile, nondestructive, rapid, and, in particular, capable of providing better insights into the physicochemical properties of substrates. First, CAM is used to characterize the surface chemistry of the substrates. We note that the acid-base properties of high surface area catalyst supports are typically determined by chemisorption. The use of chemisorption for low surface area materials, such as flat substrates used for CNT carpet growth, is challenging. For polymer films and flat substrates, CAM allows determination of the acid-base properties.[35,36] Our initial experiment confirms that CAM is a reliable approach for quantitative characterization of the acid-base properties of flat catalyst substrates.[37] With the recent advances in high-speed cameras, CAM of microdroplets has become even more reliable in characterizing the acid-base surface properties of films.[38,39] Second, XRR is used to probe the structural properties such as density, thickness, number of layers, and microscopic roughness at the surface of the substrates. Unlike transmission electron microscopy (TEM), which requires destructive sample preparation and only provides information about a limited area of the sample, or ellipsometry that depend largely on the accuracy of user-defined material properties that are usually assumed or unknown, XRR is a parameter-free approach that can be conducted without any sample preparation, damage or knowledge of the material properties.[40] The acid-base properties determined by CAM and the structural properties determined by XRR have been used to establish clear correlations between carpet growth behavior and the physicochemical properties of the substrate. A detailed discussion on the implications of the structural and acid-base properties of the catalyst substrates for CNT carpet growth is presented.

THEORETICAL BACKGROUND

Contact Angle Measurement (CAM). The contact angle (θ) formed for a drop of liquid on a flat substrate is a quantitative representation of the intrinsic ability of a non-reactive liquid to spread on a plane solid surface – a measure of the underlying competition between the energy of cohesion of the liquid molecules and the energy of adhesion between the substrate and the liquid droplet. The interfacial tensions (γ) are related to θ by the Young's equation:[41]

$$\gamma_L \cos\theta = \gamma_S - \gamma_{SL} \tag{1}$$

where γ_L, γ_S, and γ_{SL} are the surface tension of the liquid, the surface tension of the solid, and the interfacial tension between the solid and the liquid. Equation 1 has only two measurable parameters: θ and γ_L. To determine γ_s, indirect methods that involve a relation between these quantities are required. Here, the van Oss-Chaudhury-Good (VOCG) approach is used to investigate the acid-base properties of the catalyst substrates.[39,42,43] As proposed by Dupré,[38] the concepts of work of cohesion (W^{coh}) and work of adhesion (W^{adh}) can be used to describe the relation between the W^{adh} occurring between the substrate and the liquid droplet. The Dupré work of adhesion, $W^{adh} = \gamma(1 + \cos\theta)$, is an important thermodynamic parameter that characterizes the wetting or bonding between interfaces involving different materials. The work of adhesion W^{adh} is known to have a nonpolar (Lifshitz-van der Waals) and a polar (acid-base) component as expressed by the Young-Dupré equation (Equation 2):

$$(1 + \cos\theta)\gamma_L = 2\left(\sqrt{\gamma_S^{LW}\gamma_L^{LW}} + \sqrt{\gamma_S^+\gamma_L^-} + \sqrt{\gamma_S^-\gamma_L^+}\right) \tag{2}$$

The equation depicts the force-balance equilibrium for a liquid droplet on a flat substrate schematically shown in Figure 1, whereby the competition between energy of liquid cohesion is represented by the left-hand side of Equation 2, while the right-hand side represents the energy of the liquid adhesion to the surface.[23] Representative microdroplet images of water, formamide (CH_3NO), and diiodomethane (CH_2I_2) on the substrate damaged with Ar^+ ion dose of 7×10^{19} cm^{-2} at an acceleration voltage of 5 kV are shown in Figure 1. Using contact angles of three different liquids, two polar (H_2O and CH_3NO) and one nonpolar (CH_2I_2), with known surface free energies (γ_L^{LW}, γ_L^+, and γ_L^-) presented in the Supplementary Information (SI Table 1), the Lifshitz-van der Waals and the acid-base components (γ_S^{LW}, γ_S^+, and γ_S^-) of the substrate surfaces, which are unknown, can be determined

X-Ray Reflectivity (XRR). XRR is widely used to determine thickness, density and roughness of multilayer stacks on different types of crystalline and amorphous materials.[44,45] The incident angle of X-rays for XRR is varied a few degrees above and below the critical angle of reflection of the material under study. For a flat surface, the reflectivity shows a sudden decrease above the critical angle in proportion to θ_X^{-4}, whereas for a rough surface, the reflectivity decays in a faster manner. Here, θ_X is the incident angle of the X-ray beam. For substrates coated with a thin film of material with dissimilar atomic density, the reflected X-rays (*i.e.* one from the interface between the substrate and the thin film, and the other from the free surface of the thin film) interfere constructively or destructively and result in an interference pattern. A Fourier analysis of the interference pattern allows extraction of the layer thickness; the atomic density and interfacial roughness are further extracted by analyzing the amplitude of the interference oscillations. Generally, the distance between these interference patterns increases with decreasing film thickness; and films with higher atomic density and lower roughness produce more reflections. The extraction of thickness, density, surface and interface roughness of a multilayer film from profiles of the measured reflectivity as a function of θ_X require recursive analysis of reflection coefficients for different interfaces within the multilayered structure. The Fourier analysis assists this recursion by providing estimates of the thickness of the different layers, and hence reduces the number of free parameters that are optimized using non-linear least squares fitting.

EXPERIMENTAL SECTION

The substrates studied were pristine and engineered c-cut sapphire substrates. Except otherwise stated, the engineered substrates were prepared by bombardment of argon ions on pristine sapphire in a ion beam sputter deposition and etching system (IBS/e) obtained for South Bay Technology. The substrates were placed directly opposite to the Ar^+ ion source (spot size ~ 3 mm) such that the beam line is perpendicular to the substrate. The ion dose for the bombardment was varied at different acceleration voltages (ranging from 3-6 kV) by varying the beam current from 1.5-5 mA for different durations (ranging from 1-33.3 min). At a particular acceleration voltage (e.g. 5 kV), the beam current was set at a fixed value (e.g. 3.5 mA) and the duration of ion beam exposure was varied (e.g. 1, 5, 10, and 14.3 min) to obtain

respective ion doses of 1.4×10^{19}, 7×10^{19}, 1.4×10^{20} and 2.1×10^{20} cm^{-2}. For this ion dose calculation, the ion dose rate was assumed to be equal to the product of the number of ions injected per unit area per second (N) and the duration of ion exposure (t); (N) was calculated using, $N = I/qA$ cm^{-2}sec^{-1}, where I, A, and q represent the beam current in amperes, the spot area of the ion beam, and the charge of an electron (1.6×10^{-19} Coulomb), respectively.

A cross-sectional sample of an ion-beam damaged, c-cut sapphire substrate was prepared by standard TEM sample liftout procedures on a FEI Nova 200 NanoLab DualBeam SEM/FIB. Bright-field images were taken on a FEI Titan Environmental TEM operating at 300 keV in order to accentuate the contrast between the damaged layers and the bulk substrate. CNT growth was performed using CVD on ion beam damaged substrates.[30] A thin film of Fe (~ 1 nm) was deposited on the substrates by ion beam sputtering and used as the catalysts for CNT growth. The catalyst samples were annealed in H_2 ambient at 585 $^\circ$C for 10 min, then rapidly cooled down to room temperature in H_2 and were immediately subjected to growth conditions using a mixture of argon, hydrogen, water and ethylene at 760 $^\circ$C for 30 min.

AFM characterization of the surfaces was carried out using a Digital Instrument Nanoscope IIIa system operating in the tapping mode with a tip curvature radius of less than 10 nm. The images acquired were flattened to remove any tilt in the image and the root-mean-square surface roughness (R_{rms}) was determined. CAMs were conducted under ambient conditions with a commercial system (Attension Theta Optical Tensiometer, Espoo, Finland) in an enclosed chamber to exclude contamination. The system is equipped with a video camera, an adjustable sample stage, and an LED light source (Figure S1). Two polar and one nonpolar liquids with known surface energy components were used for CAM (Table S1): deionized water, diiodomethane (99% purity, from Aldrich), and formamide (99.5% purity, from Aldrich). The advancing contact angles (θ) for the different liquids were measured immediately after ion beam bombardment. The experimental procedure involved dispensing a small drop (0.5 –1.0 µL) of the test liquid on the substrate. The drop shape and θ profile were monitored with the digital camera during deposition and fluid evaporation process, and the drop diameter, left and right contact angles and volume were recorded. The sample stage was rotated to ensure that a clean surface was tested for each experiment. The drop images obtained were processed using the OneAttension software on the system and the contact angles were determined using the Young–Laplace equation to mathematically describe the drop contour. The contact angles

formed by the microdroplets were the equilibrium values calculated as the mean of measurements from at least seven droplet experiments (Table 1).

The XRR measurements were carried out in air using Rigaku-Smartlab X-ray diffractometer equipped with a Cu Kα ($\lambda = 0.154$ nm) radiation source using a slit collimation. For these X-ray measurements, precision alignment of the ion beam damaged samples was performed using rocking curves (ω scans) on the sapphire reflection. XRR was first conducted on the pristine sapphire substrate to extract its atomic density, which yielded ~ 3.99 g/cc (Figure S2a). This atomic density obtained was subsequently used as a fixed value for the substrate, enabling the extraction of structural parameters (such as layer thickness and atomic density) via least squares fitting in the "GlobalFit" thin-film analysis software.[44] Fourier analysis of reflectivity data obtained from the damaged sapphire surfaces suggest the presence of two layers on top of crystalline sapphire. Figure S2b-c confirms the uniqueness of this double layer fitting in extracting the structural parameters.

RESULTS AND DISCUSSION

The efficiency of a substrate stems from its ability to yield CNT carpets from supported Fe catalysts and it is generally quantified by recording the average height of the carpet using scanning electron microscopy. Fe catalysts placed on pristine c-cut sapphire substrate did not yield carpet growth, while the same catalysts deposited on ion beam damaged substrates or "engineered substrates" yielded significant CNT carpet growth. Substrates prepared using doses of 1.4×10^{19}, 7×10^{19}, 1.4×10^{20} and 2.1×10^{20} Ar$^+$ ions/cm^2 at 5 kV accelerating voltage yielded carpet heights of 881, 923, 1088, and 1124 μm, respectively, indicating an increase in carpet height with increasing ion dose. CNT growth details at these and other ion beam conditions have been reported previously.[30] In the following, a combination of CAM and XRR is used to characterize the physicochemical properties of the pristine and engineered substrates, and thus enabling correlations between the substrate and the growth properties. We used CAM to isolate changes in the acid-base properties (surface energy components) of substrates with distinct differences in their growth efficiency. We chose three sets of substrates prepared using ion doses of 0, 0.7×10^{20} and 1.4×10^{20} ions/cm^2 and performed CAM and CNT growth on all of them. To understand structural properties, we performed XRR on the three sets used above and,

additionally, on three more sets. Finally, TEM was used to confirm the accuracy of the XRR measurements.

Surface Topography and Acid-Base Properties. As emphasized by the Wenzel relation,[46] there is a strong influence of the surface topography and geometry on the contact angle formed by a sessile liquid drop on a plane surface. As a result, the use of CAMs for determining the acid-base properties of surfaces is limited to surfaces with identical surface topographies or surface roughness (R_{rms}) values. To verify the topographic homogeneity of the surfaces, AFM was used to characterize the surfaces; representative 3D images (500×500 nm^2) of pristine and engineered substrates are presented in Figure 2. The topographies have R_{rms} values (shown above each image in Figure 2) in the range of $0.1 - 0.4$ nm with apparent surface homogeneity. The R_{rms} values, defined as the standard deviation of the heights in the analysis area for the substrates, for all the surfaces are in the subnanometer range, which suggests that the effect of surface roughness on the contact angles is negligible – an assumption that is supported by previous studies.[47,48] We therefore conclude that the change in the contact angle observed for the various surfaces in Table 1 is primarily due to the surface chemistry and interfacial properties of the substrates, and not the surface roughness.

To characterize the acid-base properties of the substrates, CAM was conducted on pristine substrates and on substrates exposed to ion doses of 0.7×10^{20} and 1.4×10^{20} ions/cm^2. These substrates were chosen for CAM as they yielded CNT carpets of distinct heights. The advancing contact angles and their respective standard deviations were used to generate a 1000 dataset with a normal distribution and the surface free energy components were extracted from each dataset with a user defined fitting routine according to Equation 2. The details of the surface energy extraction procedure are presented in the Supplementary Information. The advancing contact angle is used in the calculations because it has been shown to be a good approximation of the Young's contact angle.[49,50] A summary of the calculated surface free energy components (γ^-, γ^+, γ^{AB}, and γ^{LW}) and the total surface free energies are summarized in Table 2, wherebythe total surface free energy (γ_S^{TOT}) is the sum of Lifshitz-van der Waals (LW) component and the acid-base (AB) component. The γ^{AB} component is further simplified in terms of the electron-accepting (γ^+) and electron-donating (γ^-) components (i.e., Lewis acidity and basicity, respectively):[39]

Nanoscale Accepted Manuscript

$$\gamma^{AB} = 2\sqrt{\gamma^+\gamma^-} \qquad\qquad (3)$$

The total surface free energies of the surfaces are between 32 and 38 mJ/m^2 with a dominant nonpolar component in the range of 27.3 – 31.4 mJ/m^2. The polar component (γ^{AB}) increases with the duration of ion beam bombardment. From Equation 5, the two contributors to γ^{AB} are the Lewis basicity (γ^-) and Lewis acidity (γ^+) and the magnitude and trends shown by these components can be used to rationalize the observed increase in γ^{AB} as the ion beam damage duration increases. It is apparent from Table 2 that even though γ^+ and γ^- increase with the duration of ion beam bombardment, γ^- is significantly higher than γ^+ for all the substrates. Thus, it can be concluded that there is a direct correlation between the ion dose, Lewis basicity of the substrate, and the growth efficiency of CNT carpet.

Interlayer Properties and Structural Evolution. A representative cross-sectional TEM image of an ion beam damaged substrate prepared using ion beam dose of $\sim 2.1 \times 10^{20}$ Ar$^+$ ions/cm^2 at a fixed accelerating voltage of 5 kV (Figure 3) shows the formation of an upper amorphous layer (Layer 1) and a lower nanocrystalline layer (Layer 2) that are formed above the crystalline sapphire. To understand the role of ion beam damage in modifying these layer properties, XRR was used to characterize the pristine and engineered substrates. Figures 4(a) and 4(b) show XRR interference pattern acquired from sapphire substrates damaged with ion beam dose of ~ 0.14-2.1×10^{20} Ar$^+$ ions/cm^2 at a fixed accelerating voltage of 5 kV and for different acceleration voltages ($\sim$3–6 kV) at a fixed damage dose ($\sim 2.1 \times 10^{20}$ Ar$^+$ ions/cm^2), respectively. The distances between the interference fringes decrease with increases in both the duration of ion beam damage [Figure 4(a)] and the acceleration voltage [Figure 4(b)], which suggests an increase in the damage depth with the increase in the degree of ion beam bombardment. Fitting the interference fringes with the theoretically generated XRR patterns reveals the presence of two layers on top of the crystalline sapphire substrate. The thicknesses of different layers probed using XRR for the ion beam damage using $\sim 2.1 \times 10^{20}$ Ar$^+$ ions/cm^2 at 5 kV is in agreement with the cross-sectional TEM image of Figure 3. This justifies the use of XRR, instead of TEM, for detailed analysis of the samples studied here. The results suggest amorphization of the surface of the substrate due to ion beam damage that continues to extend deeper into the substrate with the increase in the degree of ion beam damage.[51]

Figure 5(a) plots the parameters (thicknesses and atomic densities of Layers 1 and 2) extracted from fitting the interference fringes with the theoretically generated XRR patterns as a function of ion beam dose for the patterns in Figure 4(a). Figure 5(b) plots the same parameters as a function of ion beam acceleration voltage at a fixed dose for the patterns in Figure 4(b). The increase in ion beam dose increases the thickness of Layer 2 that is formed right above the crystalline sapphire substrate, while keeping the thickness of the top-most amorphous layer (Layer 1) roughly constant. Conversely, extracted atomic density for Layer 2 is significantly below the stoichiometric atomic density (~ 3.99 g/cc) of sapphire, while that for Layer 1 stays close to stoichiometry. The increase in the atomic density of layer 2 with increasing damage duration suggests recrystallization of the Layer 2 due to the potential increase in lattice temperature. An evidence of this increase in the lattice temperature with the increase in the degree of ion beam damage is confirmed from the shift in X-ray diffraction peaks towards a higher number (Figure S3). The increase in diffraction peaks with the increase in ion beam damage allows us to calculate the change in the distance between the crystallographic planes of the substrate ($d_{hkil} = 1/\sqrt{[4/3a^2(h^2+k^2+hk)+l^2/c^2]}$; where a and c are lattice constants and h, k, $i =$ $-h$-k, l are miller indices of sapphire.[52] As sapphire has peaks around $2\theta_X \sim 42^o$ from the (0006) plane, we have $d_{hkil} = c/6$. The shift in diffraction peaks, therefore, allows calculation of changes in the lattice constant c and hence the strain on the lattice. At the highest degree of ion beam damage we estimate a residual strain up to ~ 0.3% in the crystalline substrate underneath Layer 2. Note that this residual strain is at the bulk of the substrate at thicknesses beyond Layers 1 and 2 probed by XRR or TEM. However, existence of residual strain in the bulk suggests significant increase in lattice temperature during ion beam damage that potentially caused the recrystallization of Layer 2 observed in XRR measurements. (Signatures of recrystallization were also observed when substrates were exposed to high temperatures during CNT growth, as discussed in Supporting Information Section S1.)

From the above XRR results, we conclude that the thickness and atomic density of Layer 1, which is formed after small duration of ion beam bombardment, remains constant for the subsequent ion beam bombardment. The catalyst-substrate interactions[25] and the 3D catalyst evolution (planar Ostwald ripening and subsurface diffusion) phenomena[21,22,28] observed in previous studies were significantly impacted by the properties of the substrate surface and subsurface (Layer 1). From the unchanging nature of the physical properties of Layer 1 with the

increase in ion beam dose, we conclude that the improved growth efficiency of the engineered catalysts is due to the change in the acid-base properties, particularly the Lewis basicity. This is further corroborated by X-ray photoelectron spectroscopy analysis on various alumina samples whereby increased hydroxyl enrichment on the surface caused by ion beam bombardment was found to correlate directly with Lewis basicity and catalytic activity.[29,30]

Our analysis, as summarized in Figure 6 therefore reveal that the Lewis basicity (and corresponding polar component) and damage depth of the substrate are critical parameters that influences the activity of the catalyst during CNT carpet growth. In general, there is improved CNT carpet growth efficiency with increasing basicity and damage depth determined before and after growth as Figure 6 and Table S2 show. A key insight revealed by our results is that if the minimum substrate porosity that supports growth is established, growth efficiency can be further improved by increasing the Lewis basicity.

This study demonstrates the importance of having an upper amorphous layer and a lower nanocrystalline layer at the surface of a substrate to support CNT carpet growth. We observe that the top amorphous layer of the catalyst support even with thicknesses as small as ~ 2 nm (Figure 5) can have the desired Lewis basicity and hence porosity for CNT growth. (Note that the magnitude of porosity in the amorphous layer and its variation for different levels of CNT growth was difficult to determine using XRR due to higher error margin for that parameter.) The property of this thin top layer dominates over the structural properties of the underlying substrate (the nanocrystalline layer and below; note that the nanocrystalline layer shows lower porosity for substrates that has better CNT growth) and controls CNT growth. Once this amorphous layer is formed, one can increase catalytic activity of the substrate using ion beam damage by increasing Lewis basicity, which correlates with the enhanced carpet growth. These results suggest that the catalyst-substrate interactions and 3D catalyst evolution are largely limited to the uppermost layer of the substrate and thus the Lewis basicity has a dominant effect and accounts for the observed differences in growth efficiency for the engineered substrates.

CONCLUSIONS

The physicochemical and structural properties of ion beam damaged sapphire substrates, which have recently been proposed as novel substrates for CNT carpet growth, have been probed using a combination of CAM and XRR. Exposing an inactive c-cut sapphire substrate to ion beam bombardment results in amorphization of the substrate, which is accompanied by changes in the physicochemical properties; this process transforms the inactive c-cut sapphire substrate to an active substrate suitable for efficient CNT carpet growth. The observed transformation is rationalized on the basis of the changes in Lewis basicity, porosity and damage depth. The results demonstrate that once the top layer of a substrate is amorphized, even up to a small thickness of ~ 2 nm, the catalytic activity can be enhanced for CNT growth by increasing the Lewis basicity. Our results, therefore, demonstrate the combined utility of CAM and XRR as a powerful tool for rational design of catalyst substrates for CNT carpet growth using a non-thermochemical approach with the goal of broadening the range of substrates that support high-quality CNT growth.

Table 1. Measured mean values and standard deviations (SD) of contact angles (in degrees) for diiodomethane (θ_D), water (θ_W), and formamide (θ_F) on pristine and ion beam bombarded sapphire supports.

Catalyst support	Contact angles (θ) mean Std. Dev. (degrees)		
	CH_2I_2 (θ_D)	H_2O (θ_W)	CH_3NO (θ_F),
As-received sapphire	55.4 ± 1.4	82.0 ± 4.9	72.5 ± 2.0
Etched sapphire 5kV, 0.7×10^{20} cm^{-2} ion dose	62.6 ± 1.6	70.5 ± 5.8	65.2 ± 3.5
Etched sapphire 5kV, 1.4×10^{20} cm^{-2} ion dose	57.2 ± 7.3	62.4 ± 10.7	59.9 ± 4.6

Table 2. Summary of the calculated surface free energy components and the total surface free energies (mJ/m^2) of pristine and ion beam damaged and sapphire samples.

Substrate	Surface free energy components and total surface free energy (mJ/m^2)				
	Nonpolar, γ^{LW}	Polar, γ^{AB}	Acidic, γ^{+}	Basic, γ^{-}	γ_{TOT}
Pristine sapphire	31.3	3.2	0.2	12.4	34.4
Etched sapphire 5kV, 0.7×10^{20} cm^{-2} ion dose	27.3	5.1	0.3	21.4	32.4
Etched sapphire 5kv, 1.4×10^{20} cm^{-2} ion dose	30.4	7.8	0.5	30.6	38.2
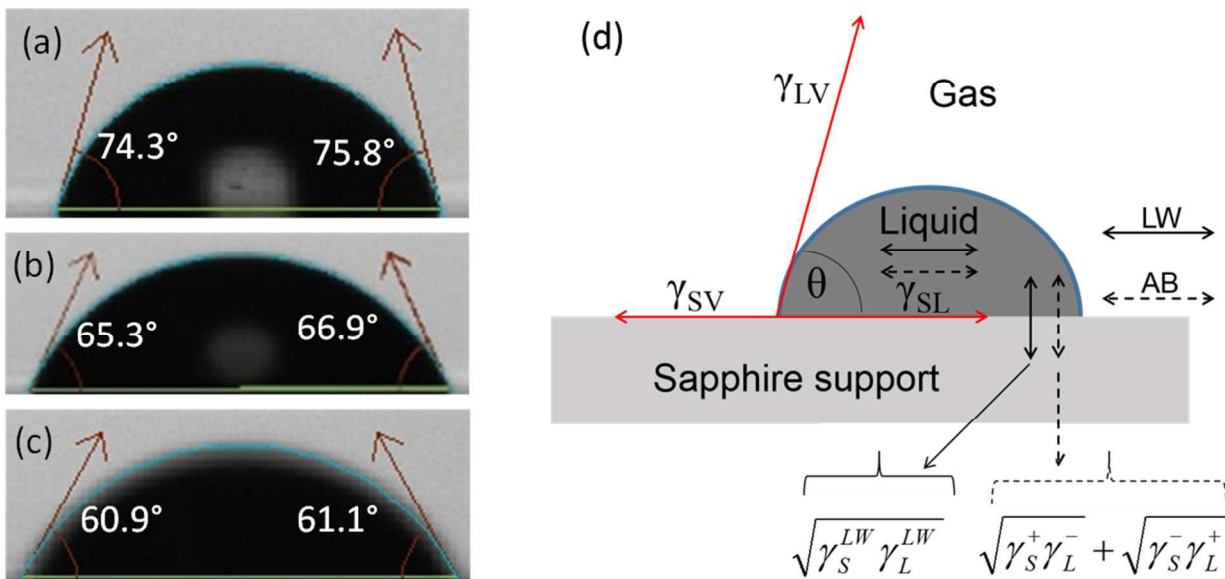
Figure 1. Representative microdroplet images of (a) water, (b) formamide and (c) diiodomethane on ion beam damaged sapphire substrates (5kV; 3.5mA, 5 min) with their corresponding left and right contact angle values. (d) A schematic of contact angle (θ) formed when the energy of cohesion between liquid molecules in the droplet is higher than the energy of adhesion between the solid surface and the liquid. The value of Cosine θ is a measure of the equilibrium between the energy of cohesion of the liquid molecules (horizontal arrows; left-hand side of Equation 2) and the energy of adhesion between the liquid and the solid (vertical arrows; right-hand side of the Equation 2). The solid and dashed arrows represent the apolar or Lifshitz–van der Waals (LW) interactions and polar or Lewis acid-base (AB) interactions, respectively.

(a) Pristine c-cut sapphire: $R_{rms} \sim 0.104$ nm

(b) 5 kV, 0.14×10^{20} cm^{-2}: $R_{rms} \sim 0.135$ nm

(c) 5 kV, 0.7×10^{20} cm^{-2} : $R_{rms} \sim 0.221$ nm

(d) 5 kV, 1.4×10^{20} cm^{-2} : $R_{rms} \sim 0.353$ nm

(e) 5 kV, 2.1×10^{20} cm^{-2} : $R_{rms} \sim 0.226$ nm
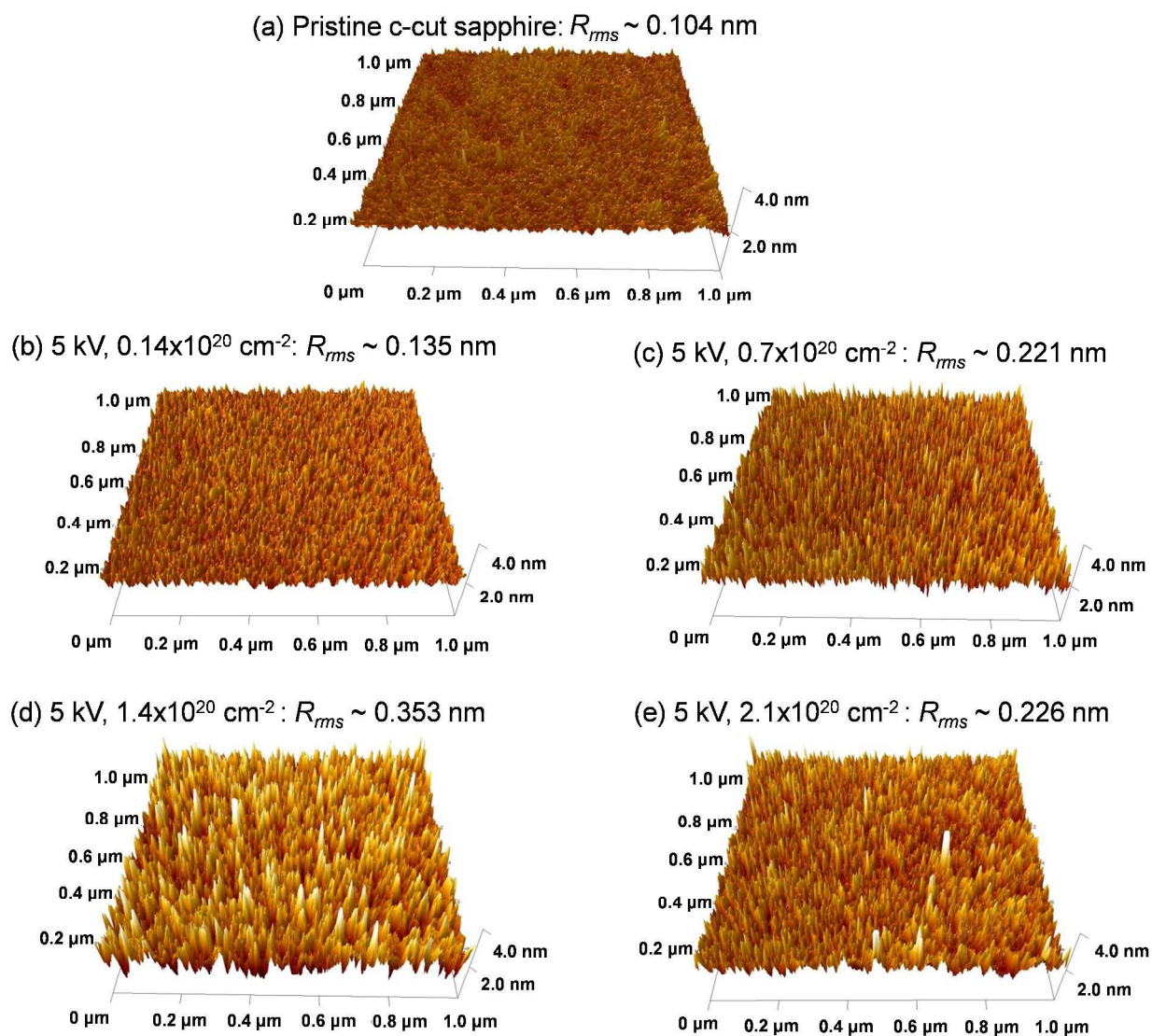
Figure 2. AFM topographic profiles of pristine and ion beam bombarded sapphire substrates at different damage conditions using 5kV accelerating voltage. The ion beam damage doses are specified above each images. The change in the surface roughness (R_{rms}) due to ion beam bombardment is low.
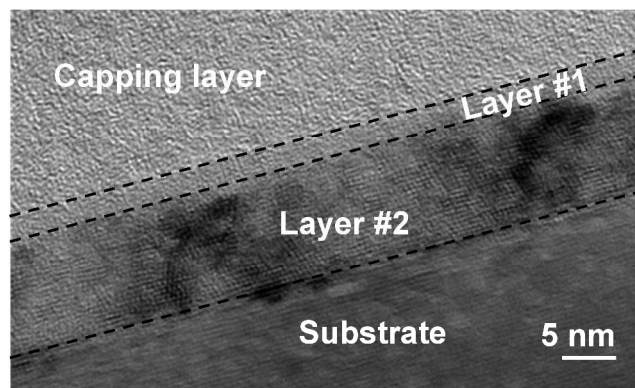
Figure 3. Cross-sectional TEM bright-field image of an ion beam damaged sapphire substrate showing the presence of an upper amorphous layer (Layer 1) and a lower nanocrystalline layer (Layer 2) on top of crystalline sapphire substrate. The dashed lines demarcate different layers and are a visual guide only. This sapphire substrate was ion beam bombarded with an ion dose of 2.1×10^{20} Ar$^+$ ions/cm^2 at 5 kV. A capping layer (carbon) was used to protect the surface during sample preparation using focused ion beam.
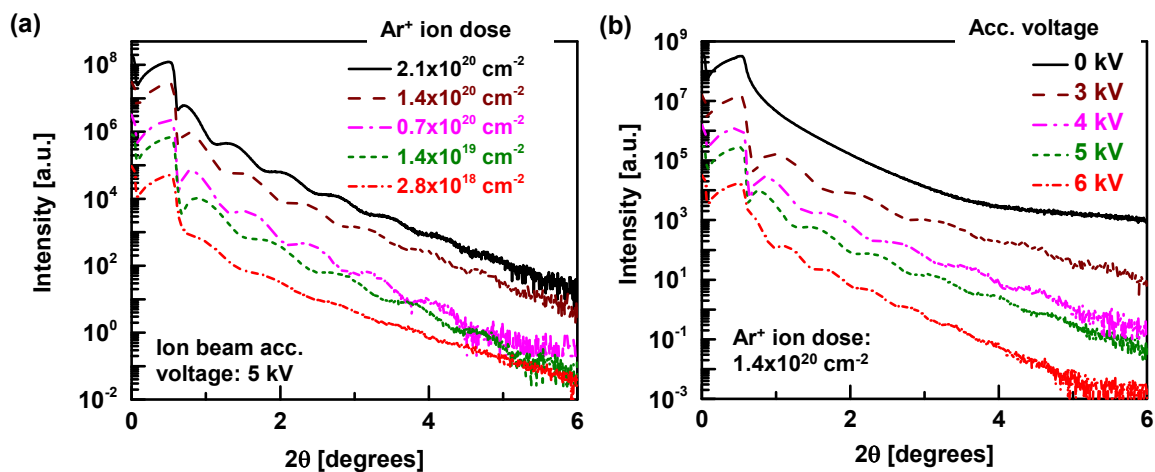
Figure 4. X-ray reflectivity (XRR) profiles of sapphire samples immediately after ion beam damage (a) at an acceleration voltage of 5 kV with various doses and (b) at various acceleration voltages for a fixed dose of 2.1×10^{20} Ar^{+} ions/cm^{2}. The XRR profile for a pristine sapphire sample (0 kV) is also shown in (b). XRR is used to determine the thickness and atomic density of different layers at the damaged surfaces.
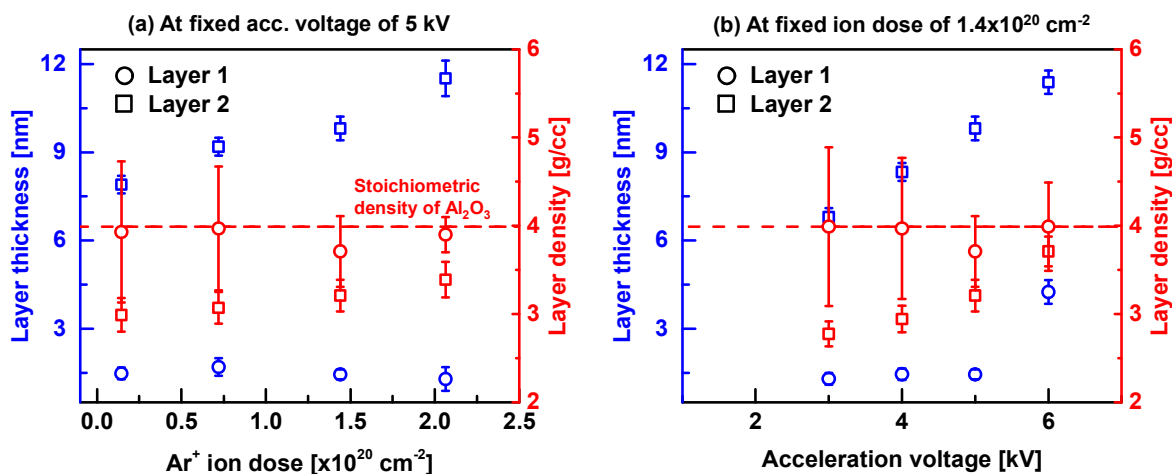
Figure 5. The thickness and the density of different layers present at the surface of ion beam damaged sapphire obtained by damaging the substrate (a) at a fixed acceleration voltage of 5 kV with varying ion doses and (b) at a fixed Ar^+ ion dose of 1.4×10^{20} cm^{-2} with varying acceleration voltage. The data in Figures (a) and (b) is obtained by fitting XRR patterns of Figures 4(a) and 4(b), respectively using a three layer model (see Supplementary Figure S2 for fitting procedures). The dashed line shows the stoichiometric density of Al_2O_3 (3.99 gm/cc).
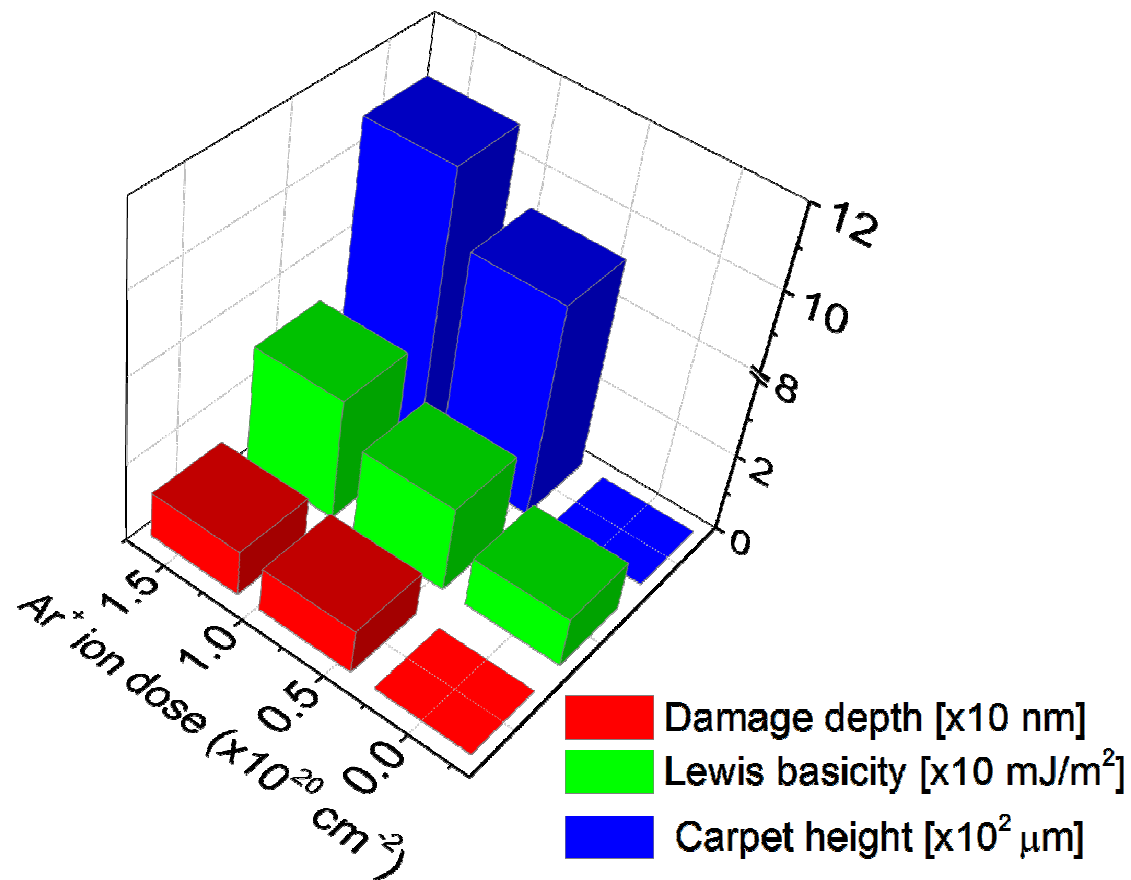
Figure 6. Effect of ion beam damage of the sapphire substrates on the Lewis basicity, damage depth of the substrate and the resulting CNT carpet height (catalyst activity). The samples were ion beam damaged at 5 kV and the corresponding ion doses after 5 and 10 min of etching were 0.7×10^{20} and 1.4×10^{20} and Ar$^+$ ions/cm^2.

Notes and References

(1) Cola, B. A.; Xu, J.; Cheng, C.; Xu, X.; Fisher, T. S. Photoacoustic Characterization of Carbon Nanotube Array Thermal Interfaces. *J. Appl. Phys.* **2007**, *101*, 054313.

(2) Cola, B. A.; Xu, X.; Fisher, T. S. Increased Real Contact in Thermal Interfaces: A Carbon Nanotube/Foil Material. *Appl. Phys. Lett.* **2007**, *90*, 093513.

(3) Xu, J.; Fisher, T. S. Enhancement of Thermal Interface Materials with Carbon Nanotube Arrays. *Int. J. Heat Mass Tran.* **2006**, *49*, 1658-1666.

(4) Futaba, D. N.; Hata, K.; Yamada, T.; Hiraoka, T.; Hayamizu, Y.; Kakudate, Y.; Tanaike, O.; Hatori, H.; Yumura, M.; Iijima, S. Shape-Engineerable and Highly Densely Packed Single-Walled Carbon Nanotubes and Their Application as Super-Capacitor Electrodes. *Nat Mater* **2006**, *5*, 987-994.

(5) Welna, D. T.; Qu, L.; Taylor, B. E.; Dai, L.; Durstock, M. F. Vertically Aligned Carbon Nanotube Electrodes for Lithium-Ion Batteries. *J. Power Sources* **2011**, *196*, 1455-1460.

(6) Li, J.; Cassell, A.; Delzeit, L.; Han, J.; Meyyappan, M. Novel Three-Dimensional Electrodes: Electrochemical Properties of Carbon Nanotube Ensembles. *J. Phys. Chem. B* **2002**, *106*, 9299-9305.

(7) Ren, Z. F.; Huang, Z. P.; Xu, J. W.; Wang, J. H.; Bush, P.; Siegal, M. P.; Provencio, P. N. Synthesis of Large Arrays of Well-Aligned Carbon Nanotubes on Glass. *Science* **1998**, *282*, 1105-1107.

(8) Lee, J.; Jung, Y.; Song, J.; Kim, J. S.; Lee, G.-W.; Jeong, H. J.; Jeong, Y. High-Performance Field Emission from a Carbon Nanotube Carpet. *Carbon* **2012**, *50*, 3889-3896.

(9) Sandler, J. K. W.; Kirk, J. E.; Kinloch, I. A.; Shaffer, M. S. P.; Windle, A. H. Ultra-Low Electrical Percolation Threshold in Carbon-Nanotube-Epoxy Composites. *Polymer* **2003**, *44*, 5893-5899.

(10) Breuer, O.; Sundararaj, U. Big Returns from Small Fibers: A Review of Polymer/Carbon Nanotube Composites. *Polym. Composite* **2004**, *25*, 630-645.

(11) Xu, X.-B.; Li, Z.-M.; Shi, L.; Bian, X.-C.; Xiang, Z.-D. Ultralight Conductive Carbon-Nanotube–Polymer Composite. *Small* **2007**, *3*, 408-411.

(12) Pint, C. L.; Kim, S. M.; Stach, E. A.; Hauge, R. H. Rapid and Scalable Reduction of Dense Surface-Supported Metal-Oxide Catalyst with Hydrazine Vapor. *ACS Nano* **2009**, *3*, 1897-1905.

(13) Hasegawa, K.; Noda, S. Millimeter-Tall Single-Walled Carbon Nanotubes Rapidly Grown with and without Water. *ACS Nano* **2011**, *5*, 975-984.

(14) Pint, C. L.; Pheasant, S. T.; Pasquali, M.; Coulter, K. E.; Schmidt, H. K.; Hauge, R. H. Synthesis of High Aspect-Ratio Carbon Nanotube "Flying Carpets" from Nanostructured Flake Substrates. *Nano Lett.* **2008**, *8*, 1879-1883.

(15) Nessim, G. D. Properties, Synthesis, and Growth Mechanisms of Carbon Nanotubes with Special Focus on Thermal Chemical Vapor Deposition. *Nanoscale* **2010**, *2*, 1306-1323.

(16) Amama, P. B.; Maschmann, M. R.; Fisher, T. S.; Sands, T. D. Dendrimer-Templated Fe Nanoparticles for the Growth of Single-Wall Carbon Nanotubes by Plasma-Enhanced Cvd. *J. Phys. Chem. B* **2006**, *110*, 10636-10644.

(17) Li, W. Z.; Xie, S. S.; Qian, L. X.; Chang, B. H.; Zou, B. S.; Zhou, W. Y.; Zhao, R. A.; Wang, G. Large-Scale Synthesis of Aligned Carbon Nanotubes. *Science* **1996**, *274*, 1701-1703.

(18) Hata, K.; Futaba, D. N.; Mizuno, K.; Namai, T.; Yumura, M.; Iijima, S. Water-Assisted Highly Efficient Synthesis of Impurity-Free Single-Walled Carbon Nanotubes. *Science* **2004**, *306*, 1362-1364.

(19) Magrez, A.; Smajda, R.; Seo, J. W.; Horváth, E.; Ribič, P. R.; Andresen, J. C.; Acquaviva, D.; Olariu, A.; Laurenczy, G.; Forró, L. Striking Influence of the Catalyst Support and Its Acid–Base Properties: New Insight into the Growth Mechanism of Carbon Nanotubes. *ACS Nano* **2011**, *5*, 3428-3437.

(20) Mattevi, C.; Wirth, C. T.; Hofmann, S.; Blume, R.; Cantoro, M.; Ducati, C.; Cepek, C.; Knop-Gericke, A.; Milne, S.; Castellarin-Cudia, C.; Dolafi, S.; Goldoni, A.; Schloegl, R.; Robertson, J. In-Situ X-Ray Photoelectron Spectroscopy Study of Catalyst−Support Interactions and Growth of Carbon Nanotube Forests. *J. Phys. Chem. C* **2008**, *112*, 12207-12213.

(21) Amama, P. B.; Pint, C. L.; Kim, S. M.; McJilton, L.; Eyink, K. G.; Stach, E. A.; Hauge, R. H.; Maruyama, B. Influence of Alumina Type on the Evolution and Activity of Alumina-Supported Fe Catalysts in Single-Walled Carbon Nanotube Carpet Growth. *ACS Nano* **2010**, *4*, 895-904.

(22) Amama, P. B.; Pint, C. L.; McJilton, L.; Kim, S. M.; Stach, E. A.; Murray, P. T.; Hauge, R. H.; Maruyama, B. Role of Water in Super Growth of Single-Walled Carbon Nanotube Carpets. *Nano Lett.* **2008**, *9*, 44-49.

(23) Wirth, C. T.; Zhang, C.; Zhong, G.; Hofmann, S.; Robertson, J. Diffusion- and Reaction-Limited Growth of Carbon Nanotube Forests. *ACS Nano* **2009**, *3*, 3560-3566.

(24) Noda, S.; Hasegawa, K.; Sugime, H.; Kakehi, K.; Zhang, Z.; Maruyama, S.; Yamaguchi, Y. Millimeter-Thick Single-Walled Carbon Nanotube Forests: Hidden Role of Catalyst Support. *Jpn. J. Appl. Phys.* **2007**, *46*, L399.

(25) Amama, P. B.; Pint, C. L.; Mirri, F.; Pasquali, M.; Hauge, R. H.; Maruyama, B. Catalyst–Support Interactions and Their Influence in Water-Assisted Carbon Nanotube Carpet Growth. *Carbon* **2012**, *50*, 2396-2406.

(26) Nguyen, J. J.; Turano, S.; Ready, W. J. The Synthesis of Carbon Nanotubes Grown on Metal Substrates: A Review. *Nanosci. Nanotechnol. Lett.* **2012**, *4*, 1123-1131.

(27) Ohno, H.; Takagi, D.; Yamada, K.; Chiashi, S.; Tokura, A.; Homma, Y. Growth of Vertically Aligned Single-Walled Carbon Nanotubes on Alumina and Sapphire Substrates. *Jpn. J. Appl. Phys.* **2008**, *47*, 1956.

(28) Kim, S. M.; Pint, C. L.; Amama, P. B.; Zakharov, D. N.; Hauge, R. H.; Maruyama, B.; Stach, E. A. Evolution in Catalyst Morphology Leads to Carbon Nanotube Growth Termination. *J. Phys. Chem. Lett.* **2010**, *1*, 918-922.

(29) Amama, P. B.; Putnam, S. A.; Barron, A. R.; Maruyama, B. Wetting Behavior and Activity of Catalyst Supports in Carbon Nanotube Carpet Growth. *Nanoscale* **2013**, *5*, 2642-2646.

(30) Islam, A. E.; Nikolaev, P.; Amama, P. B.; Saber, S.; Zakharov, D.; Huffman, D.; Erford, M.; Sargent, G.; Semiatin, S. L.; Stach, E. A.; Maruyama, B. Engineering the Activity and Lifetime of Heterogeneous Catalysts for Carbon Nanotube Growth Via Substrate Ion Beam Bombardment. *Nano Lett.* **2014**, *14*, 4997-5003.

(31) Murakami, Y.; Chiashi, S.; Miyauchi, Y.; Hu, M.; Ogura, M.; Okubo, T.; Maruyama, S. Growth of Vertically Aligned Single-Walled Carbon Nanotube Films on Quartz Substrates and Their Optical Anisotropy. *Chem. Phys. Lett.* **2004**, *385*, 298-303.

(32) Kim, S.; Pint, C.; Amama, P.; Zakharov, D.; Hauge, R.; Maruyama, B.; Stach, E. Understanding Growth Termination of Single-Walled Carbon Nanotube Carpets by Documenting the Evolution of Catalyst Morphology with the Transmission Electron Microscope. *Microsc. Microanal.* **2009**, *15*, 1176.

(33) Kim, S. M.; Pint, C. L.; Amama, P. B.; Hauge, R. H.; Maruyama, B.; Stach, E. A. Catalyst and Catalyst Support Morphology Evolution in Single-Walled Carbon Nanotube Supergrowth: Growth Deceleration and Termination. *J. Mater. Res.* **2010**, *25*, 1875-1885.

(34) Kim, S. M.; Pint, C. L.; Amama, P. B.; Zakharov, D. N.; Hauge, R. H.; Maruyama, B.; Stach, E. A. Exploiting Environmental Transmission Electron Microscopy Approaches to Understand the Origin of Carbon Nanotube Growth Termination. *Microsc. Microanal.* **2010**, *16*, 306-307.

(35) Fowkes, F. M. Quantitative Characterization of the Acid-Base Properties of Solvents, Polymers, and Inorganic Surfaces. *J. Adhesion Sci. Technol.* **1990**, *4*, 669-691.

(36) McCafferty, E.; Wightman, J. P. Determination of the Acid-Base Properties of Metal Oxide Films and of Polymers by Contact Angle Measurements. *J. Adhesion Sci. Technol.* **1999**, *13*, 1415-1436.

(37) Deshmukh, R. R.; Shetty, A. R. Comparison of Surface Energies Using Various Approaches and Their Suitability. *J. Appl. Polym. Sci.* **2008**, *107*, 3707-3717.

(38) Van Oss, C. J.: Interfacial Forces in Aqueous Media. CRC Press, Taylor & Francis Group: Boca Raton, FL, 2006.

(39) Van Oss, C. J.; Chaudhury, M. K.; Good, R. J. Interfacial Lifshitz-Van Der Waals and Polar Interactions in Macroscopic Systems. *Chem. Rev.* **1988**, *88*, 927-941.

(40) Stearns, D. G.; Gaines, D. P.; Sweeney, D. W.; Gullikson, E. M. Nonspecular X-Ray Scattering in a Multilayer-Coated Imaging System. *J. Appl. Phys.* **1998**, *84*, 1003-1028.

(41) Young, T. An Essay on the Cohesion of Fluids. *Philos. Trans. R. Soc. Lond.* **1805**, *95*, 65-87.

(42) Van Oss, C. J.: *Interfacial Forces in Aqueous Media*; 2nd ed.; CRC Press, Taylor & Francis Group: Boca Raton, FL, 2006.

(43) Ma, X.; Wigington, B.; Bouchard, D. Fullerene C60: Surface Energy and Interfacial Interactions in Aqueous Systems. *Langmuir* **2010**, *26*, 11886-11893.

(44) Yasaka, M. X-Ray Thin-Film Measurement Techniques V. X-Ray Reflectivity Measurement. *Rigaku J.* **2010**, *26*.

(45) Fujii, Y. Recent Developments in the X-Ray Reflectivity Analysis for Rough Surfaces and Interfaces of Multilayered Thin Film Materials. *J. Mater.* **2013**, *2013*, 20.

(46) Wenzel, R. N. Resistance of Solid Surfaces to Wetting by Water. *Ind. Eng. Chem.* **1936**, *28*, 988-994.

(47) Busscher, H. J.; van Pelt, A. W. J.; de Boer, P.; de Jong, H. P.; Arends, J. The Effect of Surface Roughening of Polymers on Measured Contact Angles of Liquids. *Colloids Surf.* **1984**, *9*, 319-331.

(48) Hitchcock, S. J.; Carroll, N. T.; Nicholas, M. G. Some Effects of Substrate Roughness on Wettability. *J. Mater. Sci.* **1981**, *16*, 714-732.

(49) Clark, M. D.; Jespersen, M. L.; Patel, R. J.; Leever, B. J. Predicting Vertical Phase Segregation in Polymer-Fullerene Bulk Heterojunction Solar Cells by Free Energy Analysis. *ACS Applied Materials & Interfaces* **2013**, *5*, 4799-4807.

(50) Clark, M. D.; Krishnamoorti, R. Dispersion of Functionalized Multiwalled Carbon Nanotubes. *The Journal of Physical Chemistry C* **2009**, *113*, 20861-20868.

(51) Linnros, J.; Svensson, B.; Holmén, G. Ion-Beam-Induced Epitaxial Regrowth of Amorphous Layers in Silicon on Sapphire. *Phys. Rev. B* **1984**, *30*, 3629-3638.

(52) Lucht, M.; Lerche, M.; Wille, H.-C.; Shvyd'ko, Y. V.; Ruter, H. D.; Gerdau, E.; Becker, P. Precise Measurement of the Lattice Parameters of [Alpha]-Al2o3 in the Temperature Range 4.5-250 K Using the Mossbauer Wavelength Standard. *J. Appl. Cryst.* **2003**, *36*, 1075-1081.

TOC GRAPHIC